

Cite this article as: Liang Weifeng, Lian Lixian, Lin Zifeng, et al. Preparation and Mechanical Properties of Bicontinuous Phase Mg-Ti Composite[J]. Rare Metal Materials and Engineering, 2023, 52(11): 3715-3722.
DOI: 10.12442/j.issn.1002-185X.20230229.

ARTICLE

Preparation and Mechanical Properties of Bicontinuous Phase Mg-Ti Composite

Liang Weifeng, Lian Lixian, Lin Zifeng, Liu Ying

College of Materials Science and Engineering, Sichuan University, Chengdu 610065, China

Abstract: Mg-Ti composite with bicontinuous phase structure was prepared by the additive manufacturing (AM) coupled with the melt infiltration. The effects of pore structure type and size parameters on the porosity and mechanical properties of AM-prepared Ti-6Al-4V (TC4) porous scaffold reinforcement were investigated. By adjusting the size parameters, both high porosity and appreciable compressive strength can be achieved for the scaffold. The strengthening effect of titanium alloy scaffold on the mechanical properties of Mg-Ti composite was investigated by analyzing the microstructure and interface bonding mechanism. Results show that the Mg-Ti composite has high compressive strength of 400 MPa, whereas its density is only $2.56 \text{ g}\cdot\text{cm}^{-3}$, presenting the potential as lightweight structural materials. The strength of Mg-Ti composite is higher than that of raw Mg-9Al-1Zn (AZ91) alloy matrix by 51%. This enhancement is attributed to the tight metallurgical bonding interface between the scaffold and the matrix, which promotes the effective transfer of load. Additionally, the mutual constraint effect caused by the bicontinuous phase structure and the fine crystal strengthening caused by the ultra-fine α' -Ti martensite in TC4 scaffold also significantly contribute to the improvement of mechanical properties. The investigation strategy in this research provides a nouveau path for the development of structural lightweight composites.

Key words: bicontinuous phase; Mg-Ti composite; additive manufacturing; mechanical property; lightweight structural material

Magnesium matrix composites (MMCs) are widely used in the automotive industry and aerospace fields due to their low density, excellent mechanical properties, good corrosion resistance, and low thermal expansion coefficient^[1-2]. The properties of MMCs are usually determined by the uniformity degree of reinforcement distribution. The applications of conventional particle- and fiber-reinforced MMCs are normally restricted by the anisotropy due to the uneven distribution of reinforcements^[3-4]. Recently, a nouveau type of MMCs with bicontinuous phase structures attracts much attention^[5], which involves the interpenetration between composite matrix and reinforcement. Both the matrix and reinforcement present the three-dimensional (3D) continuous distribution^[6]. Owing to the 3D continuity and symmetry of reinforcements, the bicontinuous phase composite shows isotropy characteristic and achieves better performance, showing great application potential^[5,7-8].

Usually, the reinforcement in the bicontinuous phase

composite should have high porosity. However, the traditional manufacture methods can barely prepare the materials with high porosity, such as foaming and powder loose sintering^[9-11]. Additive manufacturing (AM), as an innovative material preparation technique, has high flexibility and forming precision, which can control the morphology, distribution, and size of porous structures during the processing^[12-14]. AM is an ideal method to prepare the scaffold with open pores and high porosity, achieving the effective production of near net shape porous components with high accuracy^[15]. Ti-6Al-4V (TC4) titanium alloy is a common material for AM, and it is more suitable than brittle ceramics as reinforcement for MMCs because of its low density ($4.51 \text{ g}\cdot\text{cm}^{-3}$), remarkable mechanical property, and good wettability with magnesium^[16-21].

In this research, TC4/Mg-9Al-1Zn (AZ91) composites with bicontinuous phase structure were prepared by selective laser melting (SLM, a specific method of AM technique) coupled with melt infiltration. The effects of pore structure type and

Received date: April 21, 2023

Foundation item: Science Fund of Sichuan Province for Distinguished Young Scholars Sichuan Science (2023NSFSC1942); National Double First-Class Universities Construction Grant of Sichuan University (2020SCUNG201)

Corresponding author: Lian Lixian, Ph. D., Professor, College of Materials Science and Engineering, Sichuan University, Chengdu 610065, P. R. China, E-mail: scu_lianyi@126.com

Copyright © 2023, Northwest Institute for Nonferrous Metal Research. Published by Science Press. All rights reserved.

size parameters on porosity and mechanical properties of TC4 porous scaffold were investigated. High porosity and appreciable mechanical properties were achieved by adjusting the size parameters of the scaffold. The microstructure and interface bonding mechanism of TC4/AZ91 composite were investigated to analyze the strengthening effect of 3D TC4 scaffold in this composite.

1 Experiment

As shown in Fig.1, three kinds of porous structural models of lattice dot were designed in this research: body-centered cubic (bcc) structure, bcc_z structure, and Truss structure. The corresponding size parameters are shown in Table 1. According to Fig.1, the apertures of these TC4 scaffolds were at millimeter-level. The SLM process parameters were as follows: laser power of 280 W, scan velocity of $1200 \text{ mm}\cdot\text{s}^{-1}$, hatching space of $140 \mu\text{m}$, layer thickness of $30 \mu\text{m}$, and the rotation angle between adjacent layers of 67° . The temperature of TC4 substrate was maintained at 120°C during SLM process.

AZ91 alloy powder and porous TC4 scaffold were placed in a graphite crucible and mixed under the protection of high purity argon atmosphere. The penetration temperature and duration were 800°C and 10 min, respectively. The specimens were air-cooled to room temperature.

Porosity was defined as the ratio of pore volume of SLMed TC4 scaffold to the total scaffold volume in this research, and it could be calculated by Eq.(1)^[22], as follows:

$$P = 1 - \frac{m}{v\rho_f} \quad (1)$$

where P is the porosity; m and v are the measured mass and

volume of TC4 scaffold, respectively; ρ_f is the density of TC4 alloy ($4.51 \text{ g}\cdot\text{cm}^{-3}$).

Relative density (RD) referred to the ratio of the measured density to the theoretical density of TC4/AZ91 composite. The higher the RD value, the better the formability and the less the internal defects of this composite. Archimedes drainage method was used to measure the actual density, and the theoretical density was calculated by the mixing law of composite, as expressed by Eq.(2) and Eq.(3)^[23-24], as follows:

$$\rho = \frac{m_1\rho_a}{m_1 - m_2} \quad (2)$$

$$\rho_t = \rho_m v_m + \rho_f v_f \quad (3)$$

where ρ and ρ_t are the actual and theoretical densities of TC4/AZ91 composite, respectively; ρ_a is the density of anhydrous ethanol at 20°C ($0.79 \text{ g}\cdot\text{cm}^{-3}$); m_1 and m_2 are the mass of composite in air and anhydrous ethanol, respectively; ρ_m and ρ_f are the densities of AZ91 matrix ($1.82 \text{ g}\cdot\text{cm}^{-3}$) and TC4 reinforcement ($4.51 \text{ g}\cdot\text{cm}^{-3}$), respectively; v_m and v_f are the volume fractions of AZ91 matrix and TC4 reinforcement, respectively. Five parallel specimens were tested and measured to determine the mean value of the actual densities of each type of specimens.

The phase composition of TC4/AZ91 composite was identified by DX-2700 X-ray diffractometer (XRD). The specimen was ground by sandpaper and then etched in 10vol% citric acid solution and Kroll's reagent to reveal the microstructure of AZ91 matrix and TC4 reinforcement. The interfacial microstructure and element distribution of composites were analyzed by JSM-7900F scanning electron microscope (SEM) coupled with energy dispersive spectroscopy (EDS).

The compressive tests were conducted by Instron 5985 electronic universal machine at loading rate of $0.5 \text{ mm}\cdot\text{min}^{-1}$. The tests were repeated three times to ensure the reliability of data. The specimens were cylinders with diameter of 10 mm and height of 12 mm.

The interface model of TC4/AZ91 composite was established by Voronoi construction method^[25]. The time step Δt was 0.005 ps. In the molecular dynamics (MD) simulation, the atomic forces among Mg-Ti-Al can be described by the embedded atom-type interatomic (EAM) potential^[26-30], which can accurately model the atom interactions in the alloy system^[31-32]. The system can be further optimized by Conjugate gradient method. Isothermal-isobaric ensemble with periodic boundary conditions was applied to control the temperature. To establish the interface between TC4 and AZ91 alloys, the specimen was heated from 10 K to 1073 K, then kept at 1073 K, and finally cooled to 298 K. MD simulation was performed through the large-scale Atomic/Molecular Parallel Simulator (LAMMPS) open-source code^[33].

2 Results and Discussion

2.1 Porosity and mechanical properties of porous TC4 scaffold

2.1.1 Effect of porous structures

The porosity of TC4 scaffolds with different porous

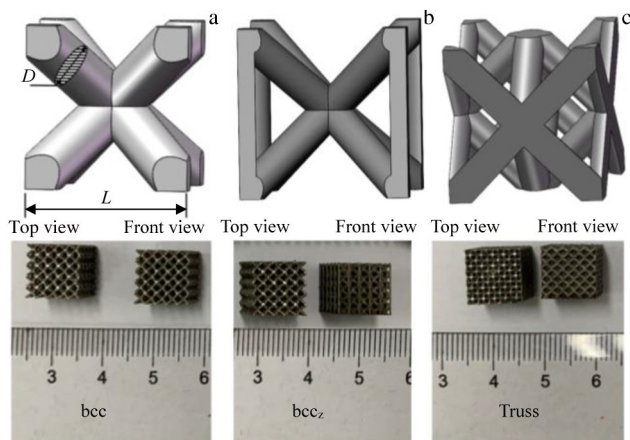


Fig.1 Schematic diagrams and appearances of bcc (a), bcc_z (b), and Truss (c) porous structural models (D denotes the cylinder diameter; L denotes the cell length)

Table 1 Size parameters of different porous structural models

| Size parameter | Porous structural model | | |
|----------------------------------|-------------------------|---------|-------|
| | bcc | bcc_z | Truss |
| Cell length, L/mm | 2 | 2 | 2 |
| Cylinder diameter, D/mm | 0.4 | 0.4 | 0.4 |

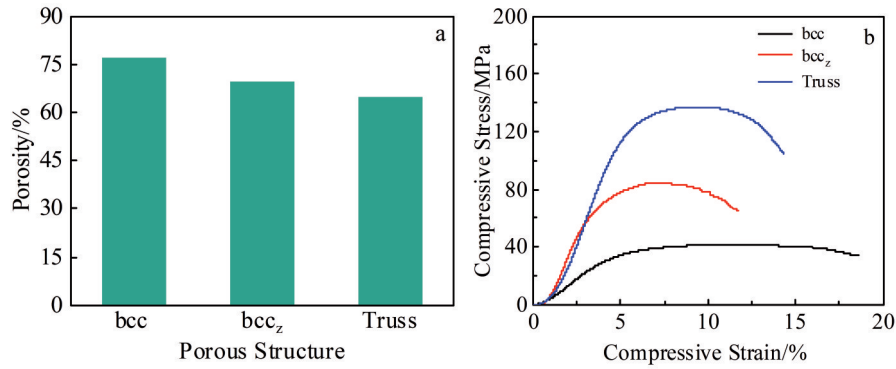


Fig.2 Porosity (a) and compressive stress-compressive strain curves (b) of TC4 scaffold with different porous structures

structures is shown in Fig.2a. The order of porosity values of TC4 scaffolds with different porous structures is $bcc > bcc_z > Truss$. The porosity of bcc scaffold exceeds 75%. According to their compressive stress-compressive strain curves (Fig.2b), all TC4 scaffolds undergo elastic deformation and plastic deformation under compressive load. With increasing the strain, the cylinder of scaffold undergoes bending and deformation to release the stress, resulting in the appearance of stress platform. Finally, the TC4 scaffold fails due to the collapse of cylinder. Therefore, the platform stress can be regarded as the maximum compressive strength of TC4 scaffolds with different porous structures, and the length of stress platform can be regarded as their capacity for plastic deformation^[34]. The order of compressive strength of TC4 scaffolds with different porous structures is $bcc < bcc_z < Truss$. Obvious stress platforms can be observed in their compressive curves: the longer the length of stress platform, the stronger the plastic deformation capacity. Therefore, the TC4 scaffold with bcc porous structure shows the optimal plastic deformation capacity. Fig.3 shows the fracture morphologies of TC4 scaffolds with different porous structures. The fracture morphology of bcc specimen is mainly composed of large and deep isodiametric dimples, indicating that a large degree of plastic deformation occurs^[34]. The dimple depth of both bcc_z and Truss specimens are shallow, suggesting that their capacities of plastic deformation are relatively worse. The fracture mechanism of these three porous TC4 scaffolds is micropore accumulation fracture.

However, high porosity leads to low compressive strength

due to the negative correlation between porosity and compressive strength. The high porosity of TC4 scaffold with bcc porous structure may degrade the mechanical properties. Therefore, it is necessary to adjust the size parameters to balance the porosity and compressive strength.

2.1.2 Effect of size parameters

The balance between porosity and compressive strength of TC4 scaffold can be achieved by adjusting the cell length (L) and cylinder diameter (D). As shown in Fig. 4a, when $L=2$ mm, the compressive strength of TC4 scaffold with bcc porous structure is gradually increased with increasing the cylinder diameter. The degree of heterogeneous deformation is decreased with increasing RD of TC4 scaffold^[35-36], resulting in the reduction of plastic deformation capability. As shown in Fig. 4b, when D increases from 0.4 mm to 0.6 mm, the strength of TC4 scaffold increases from 40 MPa to 100 MPa, whereas the porosity only declines by about 7%. A sharply negative relationship between the compressive strength and porosity can be observed when D further increases to 0.8 mm. Although the scaffold has a high compressive strength, its low porosity is not conducive to the synthesis of subsequent composite. Thus, the optimal cylinder diameter is 0.6 mm.

Under the fixed condition of cylinder diameter as 0.6 mm, the compressive stress of TC4 scaffold with bcc porous structure is gradually decreased with increasing the cell length L , as shown in Fig.5a. As shown in Fig.5b, the compressive strength significantly decreases and the porosity increases, when L increases from 1.7 mm to 2.0 mm. The compressive strength and porosity decline with further increasing the L

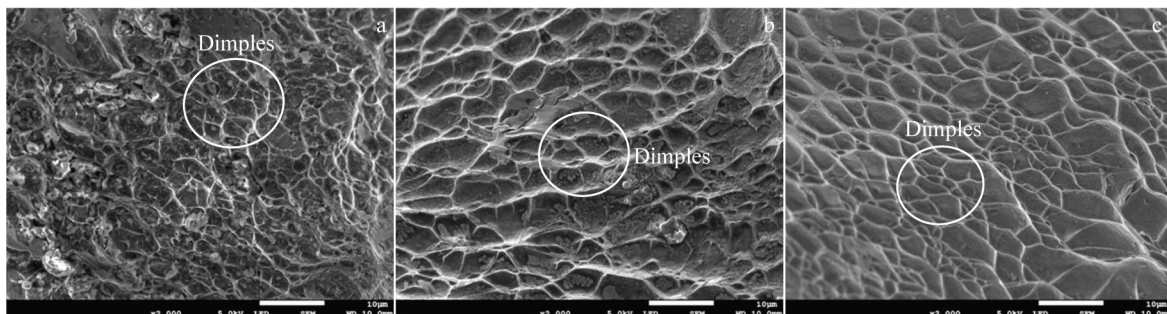


Fig.3 Fracture morphologies of TC4 scaffolds with bcc (a), bcc_z (b), and Truss (c) porous structures

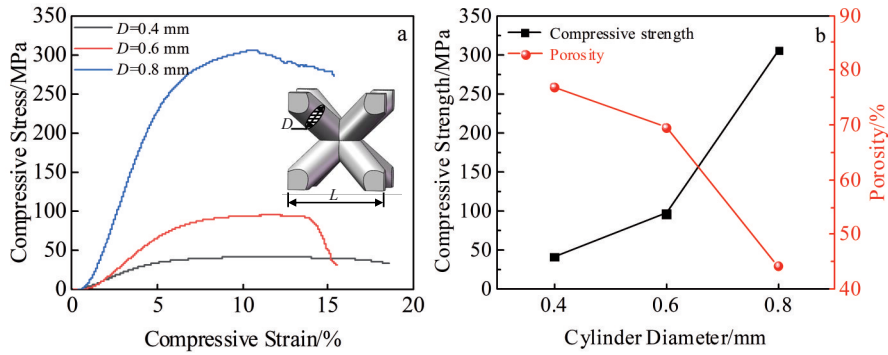


Fig.4 Effects of cylinder diameter on compressive strength and porosity of TC4 scaffold with bcc porous structure: (a) compressive stress-compressive strain curves; (b) compressive strength and porosity

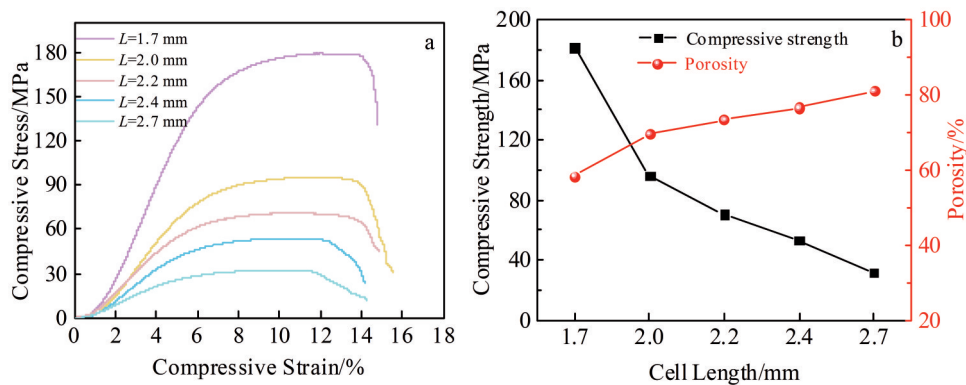


Fig.5 Effects of cell length on compressive strength and porosity of TC4 scaffold with bcc porous structure at $D=0.6$ mm: (a) compressive stress-compressive strain curves; (b) compressive strength and porosity

value, exhibiting an obviously negative relationship between porosity and compressive strength. Therefore, the optimal cell length is 2.0 mm for TC4 scaffold with bcc porous structure.

Based on these results, the optimal cylinder diameter and cell length are determined as 0.6 and 2.0 mm, respectively. In this case, the TC4 scaffold with bcc porous structure has the porosity of 70% and the compressive strength of 100 MPa, and it was used for the following analyses.

2.2 Microstructure and mechanical properties of TC4/AZ91 composite

The TC4 scaffold with optimal bcc porous structure and AZ91 magnesium alloy were used to synthesize the bicontinuous phase TC4/AZ91 composite by melt infiltration. The actual and theoretical densities of fabricated composite is about 2.56 and 2.64 $\text{g}\cdot\text{cm}^{-3}$, respectively. The high RD of 97% manifests that the as-prepared bicontinuous phase composite has excellent formability. Fig.6 shows XRD patterns of TC4 alloy, AZ91 alloy, and TC4/AZ91 composite. The phase composition of TC4/AZ91 composite is α -Mg, β - $\text{Mg}_{17}\text{Al}_{12}$, and α -Ti. No other diffraction peaks can be detected, indicating that no obvious phase reaction occurs during the infiltration process.

The appearance and microstructures of TC4/AZ91 composite are shown in Fig. 7. AZ91 matrix is sufficiently

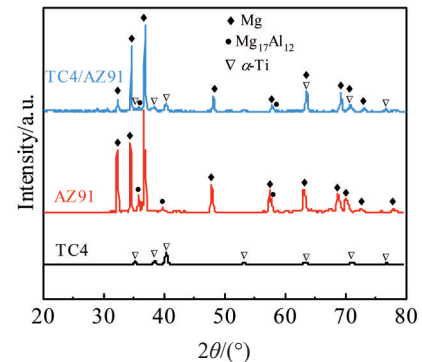


Fig.6 XRD patterns of TC4 alloy, AZ91 alloy, and bicontinuous phase TC4/AZ91 composite

permeated into the pores of TC4 scaffold (Fig. 7a). TC4 and AZ91 alloys penetrate each other in space, maintaining the continuity of their own structures and composition and exhibiting the characteristics of bicontinuous phase. A strong mutual constraint effect occurs between the matrix and the reinforcement in this unique structure, which restricts the deformation of the matrix in 3D directions, thus improving the resistance against the plastic deformation^[37-38]. Meanwhile, the continuity of TC4 scaffold can prevent the crack propagation

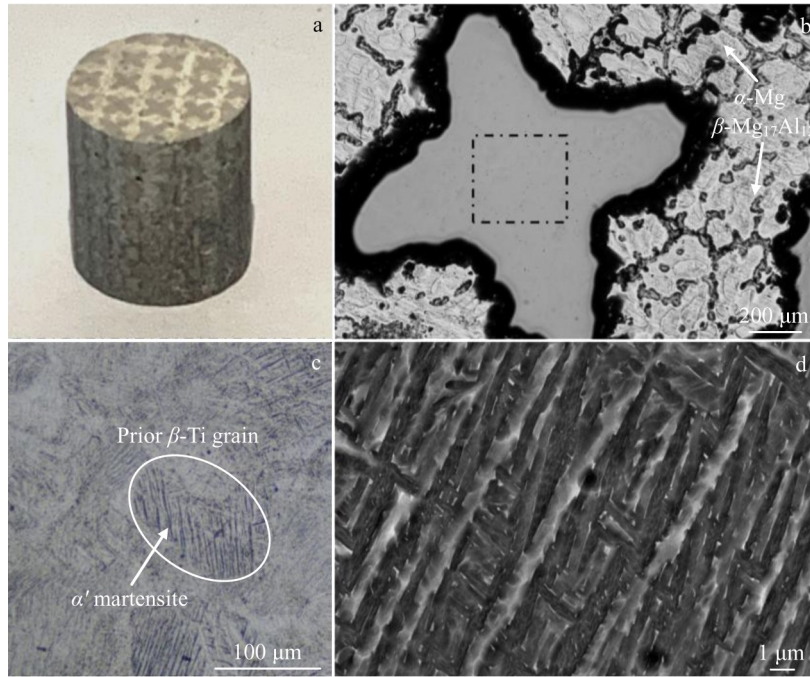


Fig.7 Appearance (a) and microstructure (b) of TC4/AZ91 composite; magnified image of the rectangle area in Fig.7b (c); magnified image of the circle area of α' -Ti needle-like martensite in Fig.7c (d)

in all directions, thereby improving the fracture resistance of composite^[39]. The microstructure of AZ91 matrix is mainly composed of bulk α -Mg and rod-like β -Mg₁₇Al₁₂, which are precipitated discontinuously along the grain boundaries. As shown in Fig. 7c, the irregular prior β -Ti grains and α' -Ti needle-like martensite are precipitated in the TC4 reinforcement. This is similar to the microstructure of TC4 alloy fabricated by SLM process, indicating that the infiltration barely has impact on the microstructure of TC4 scaffold. Thus, the ultra-fine α' -Ti needle-like martensite is preserved after compounding (Fig. 7d). These needle-like martensite can significantly inhibit the plastic deformation of TC4 scaffold due to the high density of dislocation entanglement and the dislocation twins within them, which contributes to the enhancement in mechanical properties^[40]. Moreover, the maximum and minimum lengths of most α' -Ti

martensite are approximately 25 and 1 μ m, respectively, demonstrating that the average grain size is at the a-few-micron level. Thus, these ultra-fine α' -Ti needle-like martensite can enhance the mechanical properties of TC4/AZ91 composite attributed to the strengthening effect of fine crystal^[41]. According to the compressive stress-compressive strain curves of raw AZ91 alloy and TC4/AZ91 composite in Fig. 8, the elastic deformation is directly transformed into the plastic deformation without significant yielding phenomenon during the compression. The compressive strength of TC4/AZ91 composite is approximately 400 MPa, which is higher than that of raw AZ91 alloy (about 265 MPa) by 51%, whereas they only have a little difference in ductility. Thus, the porous TC4 scaffold has a reinforcement effect on the composite without decreasing the plastic deformation capacity.

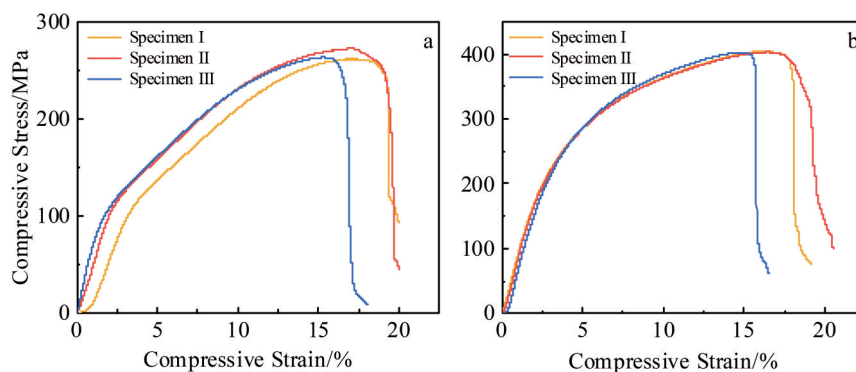


Fig.8 Compressive stress-compressive strain curves of raw AZ91 alloys (a) and TC4/AZ91 composites (b) (specimen I–III indicate the parallel specimens of each test)

Fig.9 shows SEM fractographs of raw AZ91 alloy and TC4/AZ91 composite after compression tests. Both raw AZ91 alloy and TC4/AZ91 composite fail due to shear. In Fig.9a and 9b, the fracture surface of raw AZ91 alloy has plenty of mutually parallel stripes and cleavage steps, which is similar to the fractograph of the matrix area of composite (Fig.9c). Thus, the primary fracture mechanism is the cleavage fracture, which is a common fracture mode in the close-packed hexagonal metals, such as Mg, Ti, and their alloys, and preferentially occurs on the dense atomic plane $\{0001\}$ [34]. The α -Mg/ β -Mg₁₇Al₁₂ interfaces are considered as the priority crack nucleation sites in the as-cast AZ91 alloys, and then the failure occurs with the cracks propagating along these interfaces [42]. But the cracks are impeded when they extend to the α -Mg/Ti and β -Mg₁₇Al₁₂/Ti interfaces. The TC4 scaffold separates the distribution of these two phases, preventing further crack propagation. Moreover, a large number of dimples appear in the TC4 scaffold (Fig. 9c and 9d),

suggesting that the localized plastic deformation occurs during the compression test. These dimples are also beneficial to hinder the failure of composite. The structural stability of TC4/AZ91 composite is ensured by porous TC4 scaffold to a certain extent. The TC4/AZ91 composite shows ductile-brittle mixed fracture.

Good interface bonding plays an essential role in the enhancement in mechanical properties of composites. Fig.10a shows the interfacial morphology of TC4/AZ91 composite. No obvious holes or cracks can be observed at the interface, indicating that TC4 scaffold is well bonded with the AZ91 matrix. Fig. 10b shows EDS line scanning results of the interface along the arrow in Fig.10a. It can be seen that no significant mutual diffusion occurs between the main Mg and Ti elements, whereas Al element is concentrated at the interface. The interface formation of the TC4/AZ91 composite was simulated by MD method, as shown in Fig. 11. Al atoms are evenly distributed in the

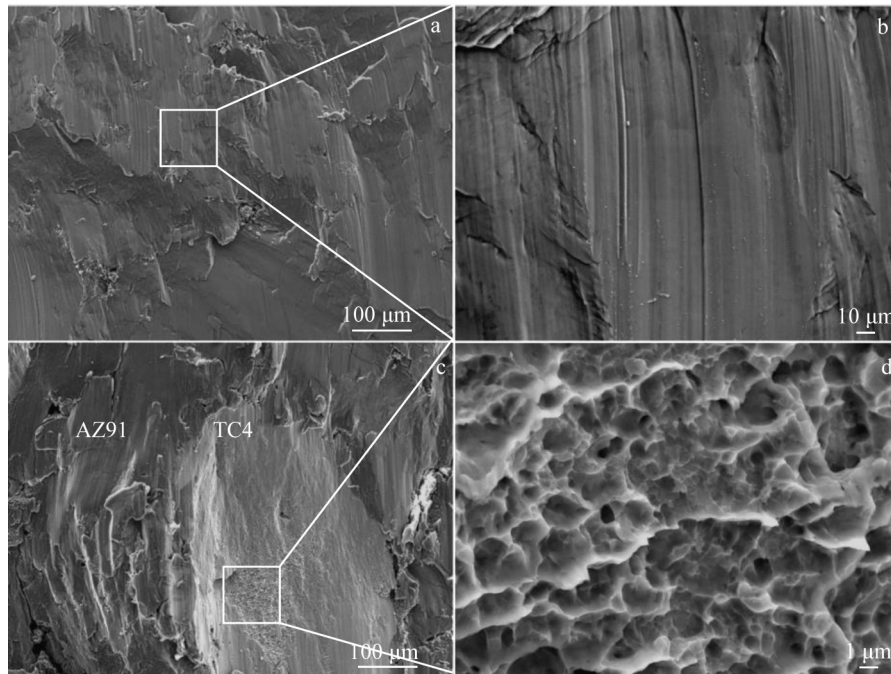


Fig.9 SEM fractographs of raw AZ91 alloy (a–b) and bicontinuous phase TC4/AZ91 composite (c–d)

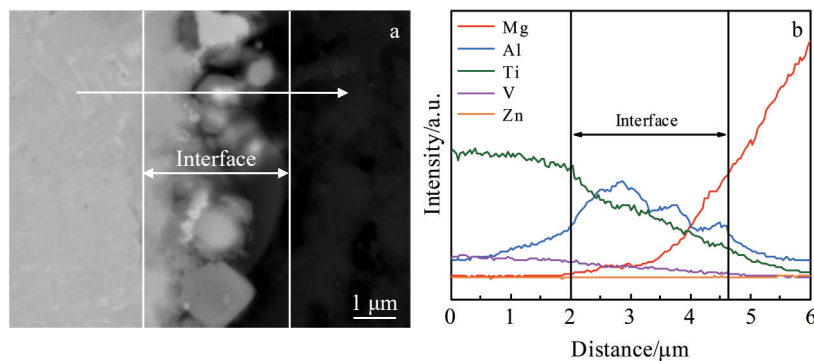


Fig.10 SEM interfacial morphology (a) and EDS line scanning results along arrow line (b) of TC4/AZ91 composite

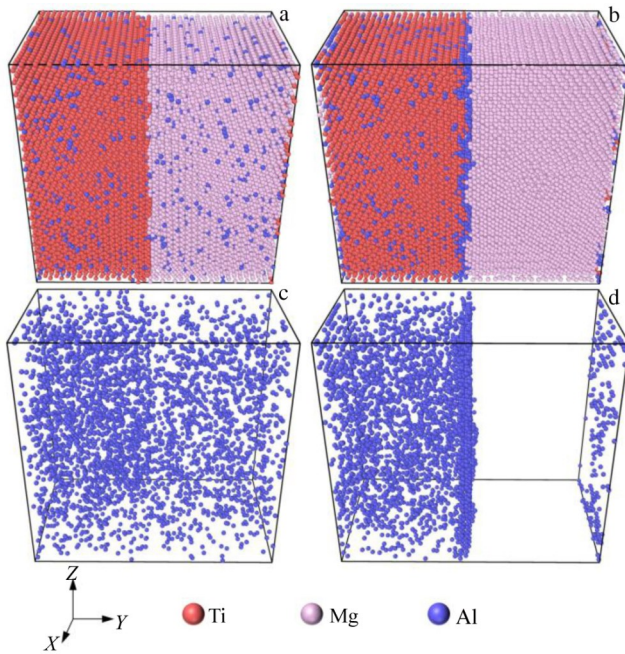


Fig.11 MD-simulated interface models (a–b) and corresponding Al distributions (c–d) of TC4/AZ91 composite before (a, c) and after (b, d) compounding

interface model of the composite before compounding (Fig. 11a and 11c). During the simulation of melt infiltration process, Al atoms are diffused and aggregated on the composite interface, as shown in Fig. 11b and 11d, which is consistent with the results from Fig. 10b. Besides, the Al atoms are basically distributed in the region of TC4 titanium alloy. It can be deduced that Al atoms in TC4 titanium alloy can hardly diffuse towards the interface due to the strong anti-segregation effect between Ti and Al^[43]. Therefore, the aggregation phenomenon of Al element at the interface is probably caused by the diffusion of Al atoms from AZ91 alloy matrix. Ref. [44] reported that the driving force of Al magnesium atoms originates from their chemical potential gradient, and the chemical potential of Al atoms is decreased with increasing the Ti mole fraction, demonstrating that Al atoms have a strong tendency to diffuse to the region with high Ti content. Compared with that in the region of AZ91 magnesium alloy, the Ti content at the interface is higher. Thus, the Al atoms in AZ91 magnesium alloy diffuse to the interface, resulting in the Al enrichment. The diffusion and aggregation of Al atoms indicate that the interfacial bonding mechanism is metallurgical bonding rather than the mechanical bonding, which has higher bonding strength and can withstand greater external load^[45]. The load borne by AZ91 matrix can be effectively transferred to the TC4 scaffold through the interface with metallurgical bonding, thereby reducing the stress concentration of the AZ91 alloy matrix. Therefore, the mechanical strength of Mg-Ti composite is significantly improved because of the interface with metallurgical bonding.

3 Conclusions

1) The body-centered cubic (bcc) porous structure is the optimal porous structure for TC4 scaffold due to its high porosity and excellent plastic deformation capacity. By adjusting the cell length and cylinder diameter of bcc porous structure, the TC4 scaffold possesses both high porosity (70%) and appreciable compressive strength (100 MPa).

2) The bicontinuous phase TC4/AZ91 composite has superior formability because of the high relative density (97%). The compressive strength of TC4/AZ91 composite is approximately 400 MPa, which is higher than that of raw AZ91 alloy by 51%. The high strength and low density (2.56 g·cm⁻³) of TC4/AZ91 composite indicate that the composite has great potential as lightweight structural materials.

3) The tight bonding of the interface between AZ91 matrix and TC4 scaffold can be attributed to the aggregation of Al element, which forms the metallurgical bonding and thus improves the efficiency of load transfer. Moreover, the mutual constraint effect caused by the bicontinuous phase structure and the fine crystal strengthening caused by the ultra-fine α' -Ti martensite also contribute to the enhancement in mechanical properties of the TC4/AZ91 composite.

References

- Zhang W, Xu J. *Materials & Design*[J], 2022, 221: 110 994
- Siengchin S. *Defence Technology*[J], 2023, 24: 1
- Nie K B, Wang X J, Deng K K et al. *Journal of Magnesium and Alloys*[J], 2021, 9(1): 57
- Jayalakshmi S, Kailas S V, Seshan S. *Composites Part A: Applied Science and Manufacturing*[J], 2002, 33(8): 1135
- Nirala A, Soren S, Kumar N et al. *Materials Today: Proceedings*[J], 2021, 46: 6587
- Kota N, Charan M S, Laha T et al. *Ceramics International*[J], 2022, 48(2): 1451
- Meenashisundaram G K, Wang N, Maskomani S et al. *Materials Science and Engineering C*[J], 2020, 108: 110 478
- Li S Q, Fu H M, Zhang H F. *Rare Metal Materials and Engineering*[J], 2014, 43(7): 1681
- Chen Y, Wang N N, Ola O et al. *Materials Science and Engineering R: Reports*[J], 2021, 143: 100 589
- Fey T, Betke U, Rannabauer S et al. *Advanced Engineering Materials*[J], 2017, 19(10): 1 700 369
- Scotti K L, Dunand D C. *Progress in Materials Science*[J], 2018, 94: 243
- Siddique S H, Hazell P J, Wang H et al. *Additive Manufacturing*[J], 2022, 58: 103 051
- Gu D D, Shi X Y, Poprawe R et al. *Science*[J], 2021, 372(6545): eabg1487
- Ngo T D, Kashani A, Imbalzano G et al. *Composites Part B: Engineering*[J], 2018, 143: 172
- Du Plessis A, Razavi S M J, Benedetti M et al. *Progress in Materials Science*[J], 2022, 125: 100 918

- 16 Kondoh K, Kawakami M, Imai H et al. *Acta Materialia*[J], 2010, 58(2): 606
- 17 Kondoh K, Kawakami M, Umeda J et al. *Materials Science Forum*[J], 2009, 618–619: 371
- 18 Zhang C L, Wang X J, Wang X M et al. *Journal of Magnesium and Alloys*[J], 2016, 4(4): 286
- 19 Liu S Y, Shin Y C. *Materials & Design*[J], 2019, 164: 107 552
- 20 Zhang F Q, Chen W G, Tian M J. *Rare Metal Materials and Engineering*[J], 2018, 47(6): 1890
- 21 Yang Z M, Wu T T, Liu J X et al. *Rare Metal Materials and Engineering*[J], 2017, 46(4): 869
- 22 Liu P S. *Titanium Industry Process*[J], 2005, 22(6): 34
- 23 Geiger A L, Walker J A. *JOM*[J], 1991, 43(8): 8
- 24 Yan X C, Chang C, Dong D D et al. *Materials Science and Engineering A*[J], 2020, 789: 139 615
- 25 Voronoi G. *Journal FÜR Die Reine und Angewandte Mathematik*[J], 1908, 1908(134): 198
- 26 Stott M J, Zaremba E. *Physical Review B*[J], 1980, 22(4): 1564
- 27 Daw M S, Baskes M I. *Physical Review B*[J], 1984, 29(12): 6443
- 28 Zhou X W, Johnson R A, Wadley H N G. *Physical Review B*[J], 2004, 69(14): 144 113
- 29 Zhou X W, Wadley H N G, Johnson R A et al. *Acta Materialia*[J], 2001, 49(19): 4005
- 30 Wadley H N G, Zhou X, Johnson R A et al. *Progress in Materials Science* [J], 2001, 46(3): 329
- 31 Zhou X W, Wadley H N G. *Journal of Applied Physics*[J], 1998, 84(4): 2301
- 32 Zhou X W, Wadley H N G. *Journal of Applied Physics*[J], 2000, 88(10): 5737
- 33 Plimpton S. *Journal of Computational Physics*[J], 1995, 117(1): 1
- 34 Pineau A, Benzerga A A, Pardoën T. *Acta Materialia*[J], 2016, 107: 424
- 35 Fatima Vaz M, Fortes M A. *Journal of Materials Science Letters*[J], 1993, 12(17): 1408
- 36 Song J, Zhou W Z, Wang Y J et al. *Materials & Design*[J], 2019, 173: 107 773
- 37 Maurya P, Kota N, Gibmeier J et al. *Materials Science and Engineering A*[J], 2022, 840: 142 973
- 38 Zhang M Y, Zhao N, Yu Q et al. *Nature Communications*[J], 2022, 13(1): 3247
- 39 Cai X C, Ding S J, Li Z J et al. *Composites Part B: Engineering*[J], 2021, 215: 108 743
- 40 Thijs L, Verhaeghe F, Craeghs T et al. *Acta Materialia*[J], 2010, 58(9): 3303
- 41 Yang J J, Yu H C, Yin J et al. *Materials & Design*[J], 2016, 108: 308
- 42 Lü Y Z, Wang Q D, Ding W J et al. *Materials Letters*[J], 2000, 44(5): 265
- 43 Kaur N, Deng C, Ojo O A. *Computational Materials Science*[J], 2020, 179: 109 685
- 44 Tan C W, Song X G, Chen B et al. *Materials Letters*[J], 2016, 167: 38
- 45 Cooke K O, Atieh A M. *Journal of Manufacturing and Materials Processing*[J], 2020, 4(2): 39

双连续相Mg-Ti复合材料的制备与力学性能

梁伟锋, 连利仙, 林紫锋, 刘 颖

(四川大学 材料科学与工程学院, 四川 成都 610065)

摘要: 采用增材制造与熔体渗透相结合的工艺制备了具有双连续相结构的Mg-Ti复合材料。研究了增材制造成形Ti-6Al-4V (TC4) 多孔骨架增强体的孔结构类型和尺寸参数对孔隙率与力学性能的影响, 使其兼具高孔隙率与良好力学强度。通过分析Mg-Ti复合材料的微观结构与界面结合机制, 探究了钛合金骨架对其力学性能的强化作用。结果表明: Mg-Ti复合材料的抗压缩强度达到400 MPa, 而其密度仅为2.56 g/cm³, 具有用作轻量化结构材料的潜力。Mg-Ti复合材料的强度与未复合的Mg-9Al-1Zn (AZ91) 合金基体相比提高了51%, 这得益于Mg-Ti两相紧密的冶金结合界面, 促进了载荷的有效传递。此外, 双连续相结构引起的相互约束效应及钛合金骨架中超细针状 α' -Ti马氏体引起的细晶强化对力学性能提升也做出了重要贡献。本研究采取的策略为复合材料的结构轻量化发展提供了新思路。

关键词: 双连续相; Mg-Ti复合材料; 增材制造; 力学性能; 轻量化结构材料

作者简介: 梁伟锋, 男, 1997年生, 硕士, 四川大学材料科学与工程学院, 四川 成都 610065, 电话: 028-85405332, E-mail: liangweifeng@stu.scu.edu.cn